Research Article Vol. 29, No. 3 / 1 February 2021 / Optics Express 4405
Optics EXPRESS

Multispectral radiometric temperature measurement algorithm for turbine blades based on moving narrow-band spectral windows

YINGZE ZHAO,[1,2] JINGUANG LV,[1,4] KAIFENG ZHENG,[1,2] JIN TAO,[1] YUXIN QIN,[1] WEIBIAO WANG,[1] CHAO WANG,[3] AND JINGQIU LIANG[1,5]

[1]*State Key Laboratory of Applied Optics, Changchun Institute of Optics, Fine Mechanics and Physics, Chinese Academy of Sciences, Changchun, Jilin 130033, China*
[2]*University of Chinese Academy of Science, Beijing 100049, China*
[3]*School of Electronic Science and Engineering and Clean Energy Materials and Equipment Center, University of Electronic Science and Technology of China, Chengdu 611731, China*
[4]*jinguanglv@163.com*
[5]*liangjq@ciomp.ac.cn*

Abstract: This paper addresses the problem of inaccurate emissivity presets for multispectral temperature measurements of aero-engine turbine blades and proposes a narrow-band spectral window moving temperature inversion algorithm that does not rely on an assumed emissivity model. As the emissivity of the measured object changes slowly over the narrow spectral window, the temperature corresponding to the normalized spectral radiation intensity for each window in the set temperature range is calculated using the Mahalanobis distance coefficient. The temperature error is less than 1.33% relative to thermocouple measurements when using this algorithm to perform temperature inversion on the experimental spectrum curves for different types of alloy samples. Furthermore, a two-dimensional spectral temperature field measurement platform was built, and the surface temperature fields of alloy samples were reconstructed using the narrow-band spectral window moving algorithm. The proposed algorithm is shown to provide high-precision inversion of the temperature field without presetting the emissivity model, which gives a new processing concept for the application of infrared spectral temperature measurements.

1. Introduction

With the development of the aviation industry, the engine thrust, specific gravity, and other performances continuously improve, which increases the operational temperature of turbine blades [1–3]. The need for accurate temperature measurements of aero-engine turbine blades is increasingly important due to reductions in their reliable working life and the material strength caused by long-term operations in extreme high-temperature and high-pressure environments [4–6]. As the traditional contact pyrometer can no longer adapt to such harsh working environments, the fast response, high upper-limit, and wide dynamic range of radiation temperature measurement technologies in the field of turbine blades have received widespread attention [7–14]. Improving the accuracy of radiation temperature measurements is important for the stable and safe operations of aero-engines.

There has been increased research on methods related to multispectral radiation temperature measurements. In 2011, Fu et al. [15] developed a fast optical fiber multi-wavelength pyrometer for 200–1700 nm wavelengths to include ultraviolet, visible, and near-infrared spectra. The optimal bandwidth and temperature discrimination method for different wavelength combinations were theoretically analyzed to improve measurement accuracies in the system. The performance

#414844 https://doi.org/10.1364/OE.414844
Journal © 2021 Received 12 Nov 2020; revised 16 Dec 2020; accepted 25 Dec 2020; published 27 Jan 2021

Optics EXPRESS

of the optical fiber multi-wavelength pyrometer was evaluated through measurements of high-temperature blackbody and molten iron. In 2014, Jordi et al. [16] used a multi-spectral pyrometer to identify the burst signals during the engine temperature measurement, and proposed a method to separate and eliminate the burst signals. In 2019, Liu et al. [17] introduced a method to estimate the combustion flame temperature and emissivity distribution from the multispectral radiation intensity, as exemplified using ethylene laminar flame temperatures. In 2016, Ketui et al. [18] simulates and studies the reflection error introduced in the temperature measurement of a single wavelength and ratio pyrometer of a rotating cooling gas turbine blade. The errors of two pyrometers under different target surface emissivity, apparent coefficient and ambient temperature are calculated. In 2017 Bouvry et al. [19] developed a multispectral radiometric thermometer to measure nuclear fuel clad zirconium alloys by assuming constant spectral emissivity in the spectral ranges of 1–1.3 μm and 1.45–1.6 μm. These measurements were in good agreement with reference thermocouple temperatures. In 2017, Manara et al. [20] built a radiation thermometer using long-wave infrared to study the surface temperature of aero-engine turbine blades. Studying the optical characteristics of the thermal barrier coating overcame the limitations of near-infrared radiation pyrometers when measuring turbine blade surface temperatures. In 2018, Wang et al. [21] used Fourier transform spectroscopy to measure the emissivity distribution of stainless steel samples over different spectral ranges and measured the real-time surface temperature of cast blanks using multi-wavelength thermometry with a bivariate emissivity function. In 2019, Lin et al. [22] proposed an improved ratio pyrometry method to analyze spectral signals and detect the emissivity distribution using Newton's iterative method to correct errors in the ratio pyrometry method by measuring the spatial distribution of the hydrocarbon flame spectra. They found a relative error for the measurements of less than 8.34% compared with thermocouple results. In 2020, Zhang et al. [23] developed a multispectral pyrometer based on a CCD array spectrometer; established a noise model for the pyrometer; evaluated the effects of readout noise, photoelectron noise, and dark noise on the accuracy of the temperature measurements; and experimentally measured maximum temperature deviations of 1% and 0.24% as introduced by photoelectron and dark noises.

These studies have made good progress in improving the temperature inversion speed and measuring the signal-to-noise ratio. However, there is no universal and accurate estimation method for emissivity models in multispectral data processing algorithms, which limits the wide application of multispectral high-temperature measurement techniques. There are currently two kinds of commonly used multispectral data processing algorithms. This first is to assume the emissivity model for the measured object surface [24–26] and introduce it into the Planck formula to solve the temperature problem. This eliminates the problem where the temperature introduced by emissivity cannot be solved. However, the emissivity is usually related to the surface topography, temperature, wavelength, and measurement angle of the object, and the calculation results obtained from the emissivity model agree with actual data, which results in large errors in the multispectral temperature measurement. The second is to transform the solution of the multi-channel temperature and emissivity into the minimum value problem of the optimization function through the simulated annealing algorithm and genetic algorithm [27,28]. Similarly, when the emissivity model deviates from that of the measured object, the solution for each channel temperature will be greatly affected.

In response to the above problems, a method based on the narrow-band spectral window moving algorithm is proposed. This approach calculates the normalized radiation intensity curve in each spectral window and compares its similarity with the standard Planck curve. The temperature distribution of the measured object is then calculated without assuming an emissivity model. Thus, a good anti-noise ability and temperature inversion efficiency are achieved. At the same time, a temperature inversion device based on a fiber optic spectrometer was established to measure the radiation spectral intensity of the object in the 900–2500 nm band. The temperatures

Optics EXPRESS

of alloy samples with different surface morphologies were measured using this method to verify the accuracy and effectiveness of the multispectral algorithm.

2. Principle of temperature measurements

2.1. Principle of radiation thermometry

The thermal radiation emitted by objects conforms to Planck's law of radiation with a radiance expressed as [29]:

$$L_b(\lambda, T) = \frac{c_1}{\lambda^5} \frac{1}{\exp[c_2/(\lambda T)] - 1}. \tag{1}$$

where $c_1 = 3.7418 \times 10^{-12}\mathrm{Wcm}^2$ and $c_2 = 1.438786\mathrm{K} \cdot \mathrm{cm}$ are radiation constants, and T is the temperature. When an optical fiber spectrometer is used to measure the temperature of the object, the radiation energy received by each channel in the spectrometer primarily includes the radiation energy of the measured object. Thus, the output response value of each channel of the spectrometer when the temperature of the object is T:

$$V(\lambda_i, T) = k(\lambda_i)\varepsilon(\lambda_i, T)L_b(\lambda_i, T) + b(\lambda_i)\ . \tag{2}$$

where $i = 1, 2, \cdots I$ is the spectral channel order of the spectrometer, I is the total number of spectral channels in spectrometer, $\varepsilon(\lambda_i, T)$ is the surface emissivity, $k(\lambda_i)$ is the radiation gain function of the optical system at the wavelength λ_i, $b(\lambda_i)$ is the radiation bias function of the optical system, which includes the thermal radiation emitted by the optical system and the detector itself, which can be obtained via blackbody radiation calibration of the optical system, and $k(\lambda_i)$ is the response value of the spectrometer.

The radiation intensity distribution in the response band of the measured object can be directly obtained from Eq. (2) as:

$$L_b(\lambda_i, T) = \frac{V(\lambda_i, T) - b(\lambda_i)}{k(\lambda_i)\varepsilon(\lambda_i, T)}. \tag{3}$$

It is seen from Eq. (3) that the I equations include $I + 1$ unknowns, unknown $\varepsilon(\lambda_i, T)$ from i channels and temperature T. The presence of the emissivity indicates the corresponding temperature solution T cannot be derived.

2.2. Spectroscopic temperature measurement algorithm for moving narrow-band spectral windows

In order to solve the problem of unsolvable temperature due to emissivity, this paper proposes a narrow-band spectral window temperature inversion algorithm, which divides the spectral response band into multiple narrow-band spectral windows, and uses the emissivity of the measured object in the narrow band The characteristic of slow change, without pre-determining the emissivity model of the temperature measurement object, the real temperature of the object can be inverted through the multi-spectral data measured by the spectrometer.

The principle of a moving solution using a narrow-band spectral window is shown in Fig. 1. Over the spectral measurement range, the wavelength points $(\lambda_1, \lambda_2, \cdots, \lambda_I)$ define the narrow interval of the spectrum for the window, which traverses the entire spectral response interval. Take any discrete spectral measurement signal $(\lambda_m, \lambda_{m+1}, \cdots, \lambda_{m+J-1})$ to form a narrow-band spectral window, in which m represents the spectral window order, J represents the spectral window width, and $m \leq I - J$. Since the spectral window width $J \ll I$, the spectral emissivity of the measured object within this narrow-band spectral window can be viewed as slowly varying. By sequentially moving the spectral window along the spectral response range, the entire spectral response interval is traversed.

Optics EXPRESS

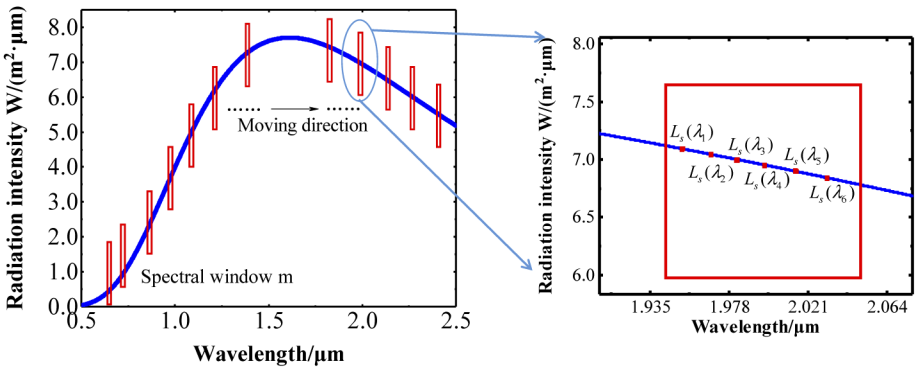

Fig. 1. Schematic diagram for the principle of the spectral window moving solution.

The spectral window contains J spectral channels, and for any spectral channel $j(j = 0, 2, \cdots J-1)$ in the spectral window, the measured spectrum is:

$$L_s(\lambda_{m+j}, T_0) = \varepsilon(\lambda_{m+j}, T_0)\frac{c_1}{\lambda_{m+j}^5}\frac{1}{\exp[c_2/(\lambda_{m+j}T_0)] - 1}. \tag{4}$$

where T_0 is the true temperature of the measured object. Within each narrow band, the radiation signal received by the spectrometer is discretized into j-dimensional vectors that form the following matrix for the measured radiation intensity:

$$Y_s(\lambda_m,T_0) = [L_s(\lambda_m, T_0), L_s(\lambda_{m+1}, T_0), \cdots, L_s(\lambda_{m+J-1}, T_0)]. \tag{5}$$

To eliminate the effect of emissivity within the narrow-band spectral window, the measurement curve within the spectral window is normalized. The normalized spectral radiation intensity matrix in the narrow-band spectral window is

$$Y_s'(\lambda_m,T_0) = \frac{Y_s(\lambda_m,T_0)}{\max[Y_s(\lambda_m,T_0)]}. \tag{6}$$

The radiant energy of the blackbody at the same temperature under different spectral channels in each narrow-band window is:

$$L_b(\lambda_{m+j}, T') = \frac{c_1}{\lambda_{m+j}^5}\frac{1}{\exp[c_2/(\lambda_{m+j}T')] - 1}. \tag{7}$$

where T' is the blackbody temperature. Construct a blackbody radiation intensity vector from Eq. (7)

$$Y_b(\lambda_m,T') = [L_b(\lambda_m, T'), L_b(\lambda_{m+1}, T'), \cdots, L_b(\lambda_{m+J-1}, T')]. \tag{8}$$

Estimate the temperature of the measured object, select and determine the upper and lower limits of the temperature inversion and the calculation step length. Setting the temperature range of T' from T_1 to T_N, so the normalized Planck radiation matrix at T_1 to T_N temperature is

$$\begin{bmatrix} Y'_b(\lambda_m, T_1) \\ Y'_b(\lambda_m, T_2) \\ \vdots \\ Y'_b(\lambda_m, T_N) \end{bmatrix} = \begin{bmatrix} \frac{L_b(\lambda_m,T_1)}{\max[Y_b(\lambda_m,T_1)]} & \frac{L_b(\lambda_{m+1},T_1)}{\max[Y_b(\lambda_m,T_1)]} & \cdots & \frac{L_b(\lambda_{m+J-1},T_1)}{\max[Y_b(\lambda_m,T_1)]} \\ \frac{L_b(\lambda_m,T_2)}{\max[Y_b(\lambda_m,T_2)]} & \frac{L_s(\lambda_{m+1},T_2)}{\max[Y_b(\lambda_m,T_2)]} & \cdots & \frac{L_s(\lambda_{m+J-1},T_2)}{\max[Y_b(\lambda_m,T_2)]} \\ \vdots & \vdots & \ddots & \vdots \\ \frac{L_b(\lambda_m,T_N)}{\max[Y_b(\lambda_m,T_N)]} & \frac{L_b(\lambda_{m+1},T_N)}{\max[Y_b(\lambda_m,T_N)]} & \cdots & \frac{L_b(\lambda_{m+J-1},T_N)}{\max[Y_b(\lambda_m,T_N)]} \end{bmatrix}. \tag{9}$$

Each row of the matrix in Eq. (9) represents the normalized standard Planck radiation intensity at different wavelengths, while each column represents the standard Planck radiation intensity

Optics EXPRESS

at different temperatures at the same wavelength. Both the value in each row and the radiation signal of the measured object can be regarded as points in the j-dimensional space. The similarity between the leaf radiation intensity curve and the standard Planck curve is defined as the distance between the spaces points between different groups, which are compared at different temperatures and calculated based on the distance similarity.

Figure 2 shows a flow chart to invert the temperature based on the spectral intensity curve. The specific solution process is as follows. In the temperature range of T_1 to T_N, the similarity distance between the two curves is defined as Eq. (10), and the similarity degree of the two curves is described. The minimized original spectrometer is used to measure the radiation curve vector and the standard Planck curve vector for the distance. The distance vector is calculated as:

$$\begin{bmatrix} d_m(T_1) \\ d_m(T_2) \\ \vdots \\ d_m(T_N) \end{bmatrix} = \begin{bmatrix} ||Y_s'(\lambda_m, T_0), Y_b'(\lambda_m, T_1)|| \\ ||Y_s'(\lambda_m, T_0), Y_b'(\lambda_m, T_2)|| \\ \vdots \\ ||Y_s'(\lambda_m, T_0), Y_b'(\lambda_m, T_N)|| \end{bmatrix}. \tag{10}$$

The Eq. (10) contains N elements, and each element represents the distance between the measured spectral intensity curve in the narrow-band spectral window and the Planck blackbody radiation curve at different temperatures. For any nth element, $n = 1, 2, \cdots N$, the Mahalanobis distance is used to measure the difference between the measured spectral radiation intensity $Y_s'(\lambda_m, T_0)$ and the standard Planck radiation intensity $Y_b'(\lambda_m, T_n)$, which effectively calculates

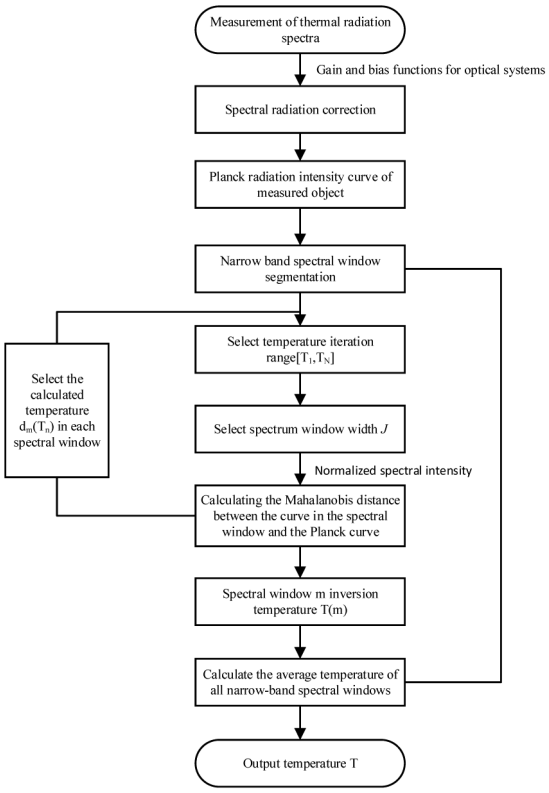

Fig. 2. Temperature inversion flow chart.

Optics EXPRESS

the similarity between two samples as

$$d_m(T_n) = \sqrt{\frac{[Y'_b(\lambda_m, T_n) - D(Y'_b(\lambda_m, T_n))] \cdot [Y'_s(\lambda_m, T_0) - D(Y'_s(\lambda_m, T_0))]}{Cov[Y'_b(\lambda_m, T_n), Y'_s(\lambda_m, T_0)]}}. \tag{11}$$

within

$$Cov[Y'_b(\lambda_m, T_n), Y'_s(\lambda_m, T_0)] = \sum_{m}^{m+J-1} L_b(\lambda_m, T_n) L_s(\lambda_m, T_0) - \frac{\sum_{m}^{m+J-1} L_b(\lambda_m, T_n) \sum_{m}^{m+J-1} L_s(\lambda_m, T_0)}{J}. \tag{12}$$

$$D[Y'_b(\lambda_m, T_n)] = \frac{1}{J} \sum_{m}^{m+J-1} L_b(\lambda_m, T_n). \tag{13}$$

$$D[Y'_s(\lambda_m, T_0)] = \frac{1}{J} \sum_{m}^{m+J-1} L_s(\lambda_m, T_0). \tag{14}$$

The greater the correlation distance $d_m(T_n)$ between the curves, the weaker the correlation between the spectral radiation intensity curves as measured by the spectrometer and the standard Planck radiation intensity curves. Conversely, a smaller distance coefficient gives a stronger correlation. When the distance between $Y'_s(\lambda_m, T_0)$ and $Y'_b(\lambda_m, T_n)$ is minimized in the mth spectral window, the temperature corresponding to $d(m) = d_m(T_n)$ is the corresponding measured temperature in the current spectral window, as shown in Fig. 3. The corresponding temperature is

$$T(m) = T|_{d(m)=\min[d_m(T_1),\ d_m(T_2), \cdots,\ d_m(T_N)]}. \tag{15}$$

The average of the calculated temperatures in all narrow-band spectral windows are taken to obtain the final inversion temperature as:

$$T = \frac{1}{I-J} \sum_{m=1}^{I-J} T(m) = \frac{1}{I-J} \sum_{m=1}^{I-J} T|_{d(m)=\min[d_m(T_1),\ d_m(T_2), \cdots,\ d_m(T_N)]}. \tag{16}$$

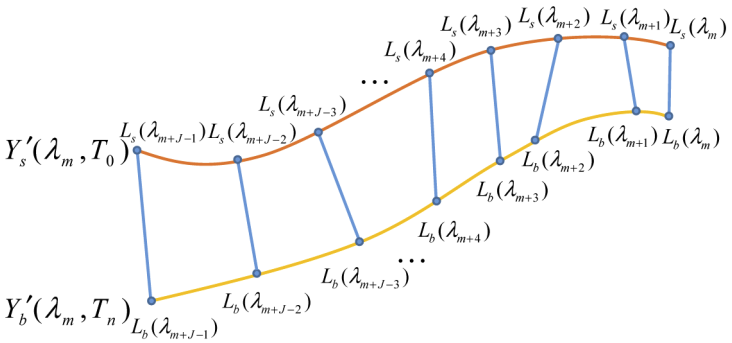

Fig. 3. Schematic diagram to calculate the similarity coefficient of two discrete curves in the narrow-band spectral window.

Optics EXPRESS

3. Simulation verification

The proposed algorithm is simulated to verify the temperature inversion accuracy of the narrow-band spectral window moving algorithm for different types of emissivity targets. Table 1 shows the four commonly used emissivity models, and Fig. 4 shows the spectral radiant intensity distribution curves at different temperatures as calculated from the emissivity models in Table 1. The emissivity model parameters of the measured target are shown in Table 2. It can be seen from Fig. 4, the same emissivity model under the measured object spectral radiation intensity curve trend, while the same temperature different emissivity model calculation of the spectral radiation intensity curve is more different. This paper takes aero-engine turbine blades as the research object for simulations and experiments to evaluate the temperature inversion accuracy of the spectral window temperature inversion algorithm.

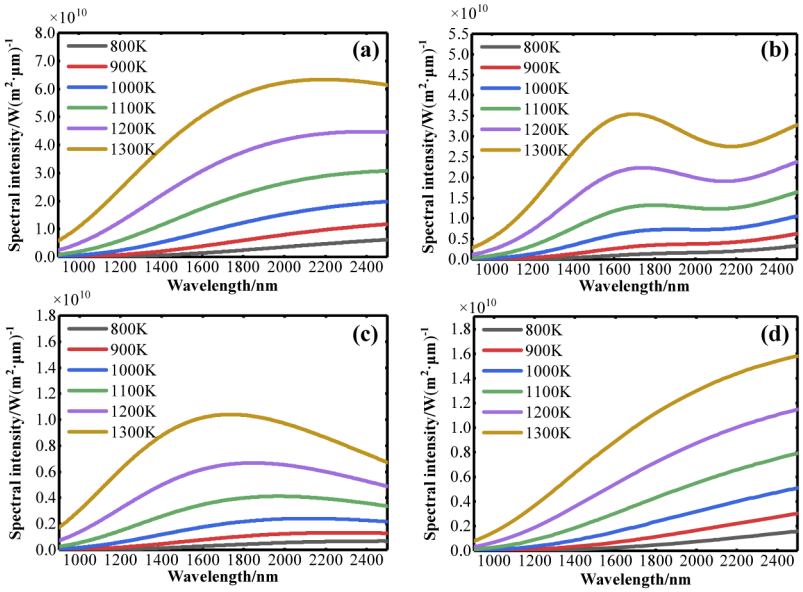

Fig. 4. Spectral radiation intensity distribution of the measured object under different emissivity models: Models (a) A, (b) B, (c) C, and (d) D.

Table 1. Target emissivity model

Target	Spectral Emissivity
Model A	$\varepsilon(\lambda) = \sum_{i=0}^{n} a_i \lambda^i$
Model B	$\varepsilon(\lambda) = a_0 + a_1 \sin(a_2 + a_3 \lambda)]$
Model C	$\varepsilon(\lambda) = \exp[-(a_0 + a_1 \lambda)^2]$
Model D	$\varepsilon(\lambda) = \exp(a_0 + a_1 \lambda)$

The principle of the narrow-band spectral window width selection depends on the emissivity trend of the measured object. When the emissivity of the object in the measurement band changes quickly, the spectral window width selection should correspondingly decrease. When the emissivity over the entire measurement band changes more slowly, the spectral window width can be wider. This paper performs radiation measurements on turbine blades. According to the emissivity distribution trends given in [30–32], the turbine blades have relatively gentle variations throughout the spectral measurement interval when the target material set temperature is 1200 K

Optics EXPRESS

Table 2. Emissivity model parameters

Parameters	Model A	Model B	Model C	Model D
a0	0.05687	0.5	−1	−3.5
a1	−0.000212	0.1	−0.0002	0.0009
a2	0	0.01	/	/
a3	0.04046×10^{-9}	0.2	/	/

and within the response band of the spectrometer of 900–2500 nm, which has a resolution of 3 nm. Therefore, the width of the spectral window is chosen as 12 nm to ensure there are sufficient calculation points within the spectral window. The spectral distribution of the radiation received by the multispectral temperature measurement system is calculated using Eq. (2). To verify the noise immunity of the algorithm, 20 and 30 dB of random noise is added to Eq. (2). Figure 5(a) shows the simulated radiation intensity spectrum line and the set emissivity model A from Table 1 after adding 30 dB of noise. Figure 5(b) shows the radiation spectrum intensity curve of the calculated temperature range along with the final inversion temperature. The method using the emissivity model and the narrow-band spectral window was used to calculate the temperature of the measured target under different emissivity models.

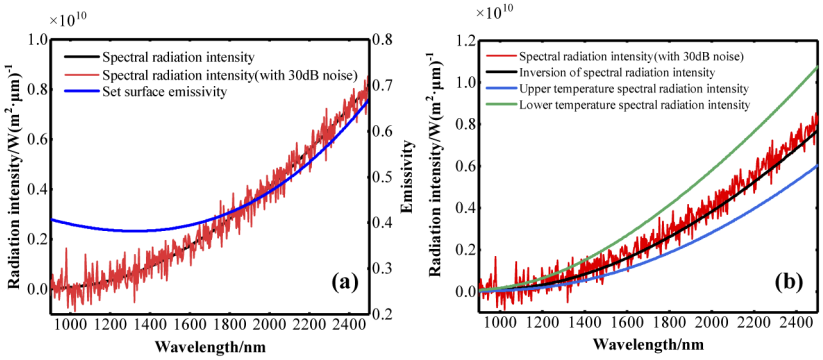

Fig. 5. (a) Spectral radiation intensity and emissivity distribution curves of the measured objects at 1200 K and (b) inversion temperature of the radiation spectrum intensity distribution curve.

The results of the temperature inversion are shown in Figs. 6(a) and 6(b), which compare the target temperature inversions using four different emissivity models (A–D in Table 1). The emissivity model algorithm solves for the target temperature by fitting its spectra to the emissivity model. When the emissivity model of the target is inconsistent with the temperature calculations, large errors occur in the temperature measurements. The narrow-band spectral window moving algorithm is used to calculate the four different spectral curve measurements. The inversion temperature is close to the modeled temperature of 1200 K with an error below 2%. This indicates that the proposed method can calculate the temperature more accurately and has good anti-noise abilities.

Optics EXPRESS

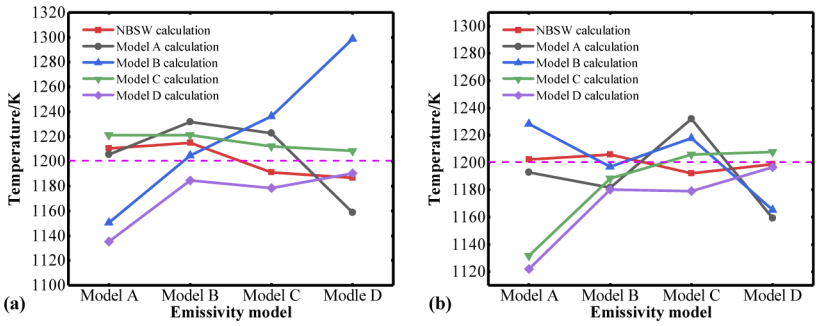

Fig. 6. Temperature simulation results with random added noise of (a) 20 and (b) 30 dB.

4. Experimental verification

4.1. Experimental platform construction

The experimental apparatus used in this paper is shown in Figs. 7 and 8. The experimental samples were the commonly used GH3030 high-temperature alloy (Ni 75%, Cr 19%, Ti 0.35%), which has good oxidation and heat resistances along with fatigue and cold stamping characteristics. The measured sample had a swallow tail structure with a length of 180 mm, a width of 40 mm at both ends, and a width of 10 mm at the narrowest point in the middle, which is where the resistance was the largest and the temperature was the highest. During the experiments, a thermocouple was welded to the surface of the alloy sample to measure the set temperature. A current heating device was used to heat the alloy sample to a set temperature, and the thermal radiation from the alloy sample was received by an optical probe after being focused by a lens and passed through an optical fiber into the spectrometer (NIRQUEST 2.5–512) with a spectral resolution is 3nm. The optical probe was moved using a two-dimensional electronically controlled displacement stage to collect the intensity of the radiation spectrum at different coordinates of the alloy sample. The displacement was controlled using a Zolix PA200 motorized displacement stage with a step resolution of 20 μm. At the same time, a cold gas purge structure was added to the probe to ensure the distance between the probe and the turbine blade to be measured was sufficiently close. Thus, the influence of the gas radiation absorption between the turbine blade and the optical path of the measurement probe on the temperature measurements can be ignored.

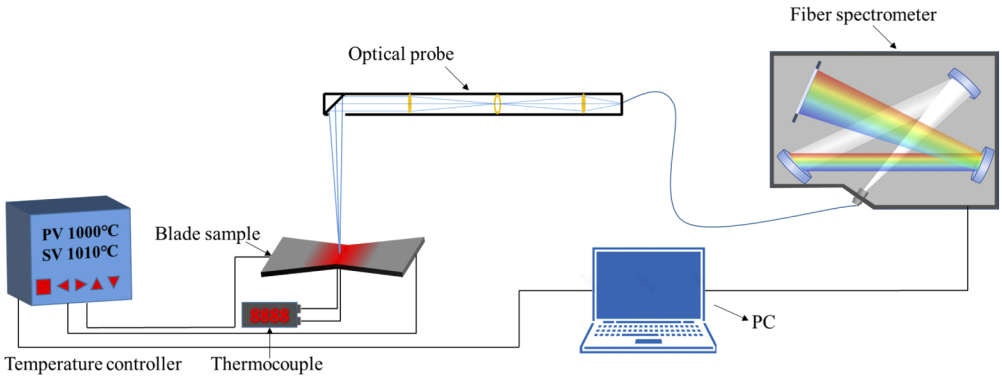

Fig. 7. Structure diagram of the experimental device for the temperature measurements of alloy samples.

Optics EXPRESS

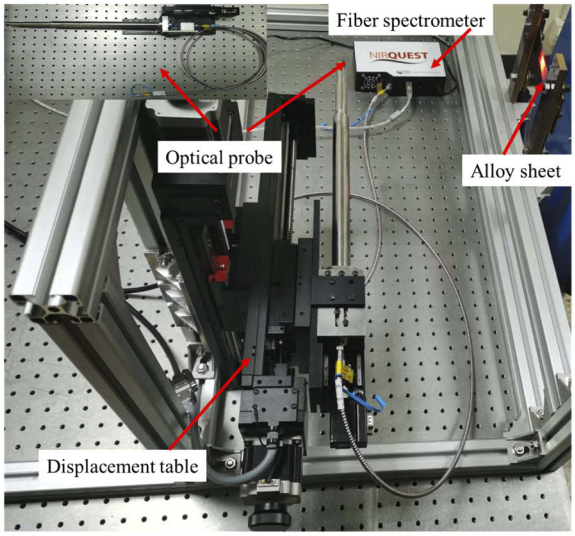

Fig. 8. Experimental diagram of the alloy sheet temperature measurements.

4.2. Spectral radiation calibration

The traditional multispectral calibration method assumes that the detector has a linear response to incident radiative light. The radiation and gain of the spectral system can be solved by measuring the radiation of high and low temperature blackbody. The use of this method has the following assumptions. First, assume that the detector responds linearly in a small range; second, assume that the emissivity of the black body is 1; third, the set black body temperature is consistent with the actual temperature, and the surface temperature is uniform. However, in actual measurements, the radiation gain and bias function of the multispectral temperature measurement system are not linear. To improve the calibration accuracy of the measurement instrumentation, this paper proposes a multi-point calibration method that simultaneously measures $P(P>2)$ blackbody temperature points. This method then corrects the radiation of the temperature-measuring spectrometer to minimize the sum of squared errors between the spectral response and the theoretically calculated response. Namely:

$$S = \sum_{p=1}^{P} [V(\lambda, T_p) - k(\lambda) \cdot L_s(\lambda, T_p) - b(\lambda)]^2 = \min . \tag{17}$$

where $p = 1, 2, \cdots P$ is the serial number for measuring the temperature of the black body furnace, $V(\lambda, T_p)$ is the response amplitude of the spectrometer, $L_s(\lambda, T_p)$ is the radiation intensity of the measured object under the measurement conditions.

The gain and bias of the optical system for the spectral temperature measuring instrument can be solved using the least squares fitting method as:

$$k(\lambda) = \frac{P \sum_{p=1}^{P} L_s(\lambda, T_p) V(\lambda, T_p) - \sum_{p=1}^{P} L_s(\lambda, T_p) \sum_{p=1}^{P} V(\lambda, T_p)}{P \sum_{p=1}^{P} [L_s(\lambda, T_p)]^2 - [\sum_{p=1}^{P} L_s(\lambda, T_p)]^2}. \tag{18}$$

$$b(\lambda) = \frac{1}{P}[\sum_{p=1}^{P} V(\lambda, T_p) - k(\lambda) \sum_{p=1}^{P} L_s(\lambda, T_p)]. \tag{19}$$

Optics EXPRESS

The blackbody radiation corrections are performed for the temperature measurement optical system. Ten standard blackbody temperature points were measured in the temperature range of 873–1273 K. The gain and offset curves of the radiation temperature measurement system were calculated using Eqs. (18) and (19). The calculation results are illustrated in Fig. 9, which shows the radiation gain of the detector is small on both sides of the response band. The spectral radiation curve of the blackbody furnace in Fig. 10(a) was corrected using the radiation gain and offset curve. The measurement curve results of the optical system after corrections are shown in Fig. 10(b).

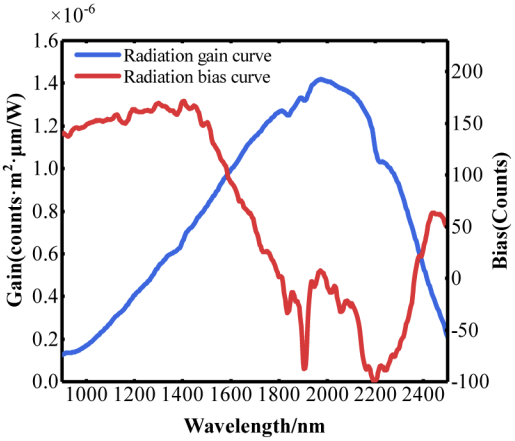

Fig. 9. Spectral gain and bias distribution curves from the radiation temperature measurement system.

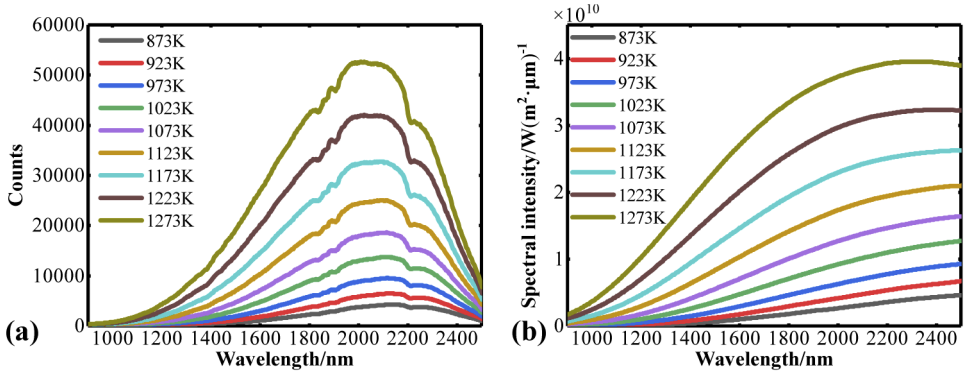

Fig. 10. (a) Measured spectrum radiation curve of a blackbody furnace from 873–1273 K and (b) measured radiation intensity curve at different temperatures after multi-point radiation corrections.

4.3. Temperature measurement of alloy samples

4.3.1. Temperature measurement of alloy samples under different roughness

Three samples with different surface morphologies were prepared after a polishing treatment of the GH3030 alloy samples to verify the temperature inversion accuracy for the narrow-band spectral window moving algorithm for samples of different surface emissivities. Figure 11 shows a schematic diagram to measure the surface roughness distribution of alloy samples using

Optics EXPRESS

laser confocal microscopy at a 20x magnification. The surface morphology is modified after polishing, and the sample surface undulations gradually decrease with an increased polishing mesh. Figure 12 shows the roughness profile curves of the three alloy samples measured using laser confocal scanning. The average arithmetic deviations R_a of the surface profiles of samples 1 to 3 are 1.319, 1.035, and 0.869 μm, respectively.

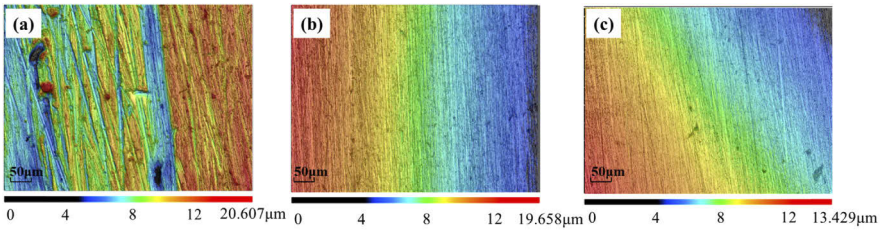

Fig. 11. Laser confocal microscopy measurements of the surface roughness distribution for samples (a) 1, (b) 2, and (c) 3.

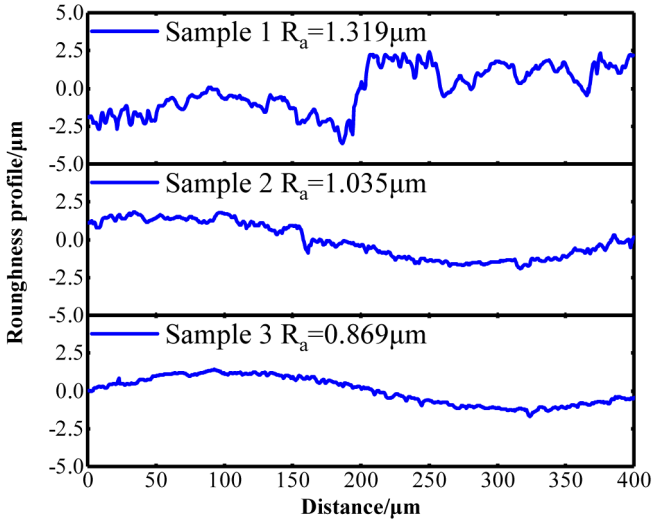

Fig. 12. Average arithmetic deviation of the surface profile distribution curve and profile of samples 1 to 3.

We used the energy comparison method to measure the emissivity of the alloy samples at different temperatures and verified that their emissivities had different distributions at various roughnesses. According to the definition of spectral emissivity, the emissivity is expressed as the ratio of the radiation emissivity of the object under test at the same temperature to that of the blackbody at the same temperature. The infrared radiation intensity of the sample under test and the blackbody furnace under the same heating temperature and environmental conditions are measured separately, and the emissivity distribution of the object under test is calculated by the ratio of the two. The emissivity distribution curves of Samples 1 to 3 at 973 and 1073 K (shown in Fig. 13) show a gradually increasing emissivity as the roughness R_a of the samples increases at the same temperature. For the same alloy roughness, the emissivity increases gradually with temperature. Similar to the conclusions from Refs. [33,34], samples with different emissivities were obtained by varying the roughness of the alloy sample surface.

Optics EXPRESS

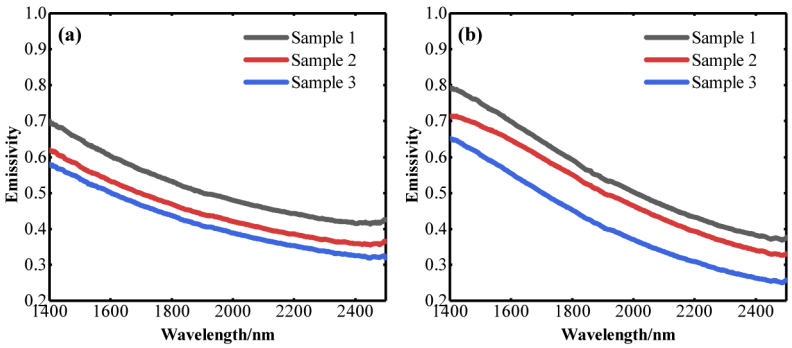

Fig. 13. Curves of emissivity versus wavelength for samples 1 to 3 at (a) 973 and (b) 1073 K.

A current heating device is used to increase the sample temperature. The temperature distributions of the alloy samples under different surface roughnesses were measured. The inversion accuracy of the narrow-band spectral window movement algorithm is verified through comparisons with a reference thermocouple. Six experimental temperature points were measured from 890–1200 K for samples 1 to 3. The radiation spectroscopy measurements for the alloy samples were collected using the multi-point temperature correction method. The narrow-band spectral window moving algorithm and the emissivity model algorithm were used together to calculate the temperature and the associated errors of the alloy sample spectral temperature measurements, as shown in Fig. 14. The relative error of the narrow-band spectral window moving temperature inversion algorithm is less than 1.17%, and the inversion results show that the algorithm has a good computational accuracy without pre-setting the emissivity model.

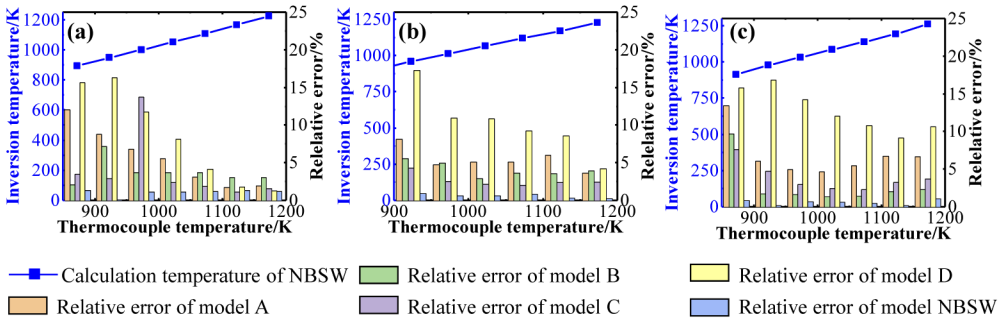

Fig. 14. Temperature inversion error distribution of alloy samples with different surface morphologies using the narrow-band spectral window moving algorithm (NBSW) and emissivity model algorithm at different heating temperatures for samples (a) 1, (b) 2, and (c) 3.

4.3.2. Temperature measurement of different types of alloy samples

To verify the accuracy of the temperature inversion determination for different alloys, three samples (DD6, DZ125, and K77) that are commonly used in the manufacture of turbine rotors and guide vanes for aero-engines were considered for the temperature measurement experiments. After surface treating the three different types of alloy samples to similar roughnesses using sandpaper, the samples were heated to six temperatures between 1023 and 1273 K to measure the spectral radiation intensities of the different alloy types. The relative errors for the temperature

Optics EXPRESS

inversions of the three samples using the narrow-band spectral window shift algorithm were less than 1.33%, as shown in Table 3.

Table 3. Temperature inversion results for the DD6, DZ125, and K77 samples

Temperature/K	1023	1073	1123	1173	1223	1273
DD6/K	1033.1	1078.4	1134.6	1188.6	1233.4	1273.5
relative error/%	0.987	0.503	1.033	1.33	0.85	0.039
DZ125/K	1034.3	1085.2	1135.0	1184.9	1225.0	1279.8
relative error/%	1.105	1.137	1.069	1.014	0.164	0.534
K77/K	1031	1084.1	1136.2	1189.8	1232.4	1278.7
relative error/%	0.782	1.034	1.175	1.432	0.769	0.448

The analysis of the experimental spectral data shows that the inversion errors for models B and C are lower than those for models A and D when the inversions are performed for different sample temperatures. As the heating temperature gradually increased from 890–1200K, the measured spectral signal-to-noise ratio increased, and the relative error of the temperature inversion for the four emissivity model algorithms decreased, where the lowest relative error was 5%. The narrow-band spectral window moving algorithm had an inversion error of less than 1.33% for the surface temperatures for alloys of different types, roughnesses, and heating temperatures. Therefore, the proposed algorithm is not limited by the emissivity of the measured object in practical measurements, which is of high practical value.

4.4. *Temperature field distribution of alloy samples*

The traditional thermocouple temperature measurement method only provides the temperature at certain points along the object. Due to the limitations of the welding volume of the thermocouple, it is difficult to completely reflect the temperature field distribution of the entire object surface. The two-dimensional spectral temperature field measurement platform system quickly scanned the entire surface of the tested alloy sample using the probe and obtained the spectral distribution. The narrow-band spectral window movement algorithm was then used to invert the surface temperature field distribution. The spectral scanning of the GH3030 alloy sample with this measurement platform yielded a hyper-spectral pseudo-color data cube that contained both spatial and spectral information from the sample, as shown in Fig. 15(a). Each coordinate point on the

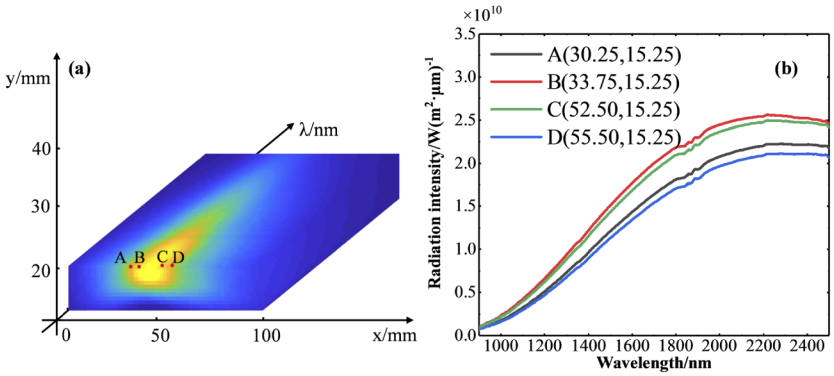

Fig. 15. (a) Hyper spectral radiance images of the surface of the half-height alloy samples under different spectral dimensions and (b) distribution of spectral intensity curves at points A-D near the center point.

Optics EXPRESS

sample surface corresponds to a set of spectral intensity data for different wavelengths, which allows calculating the temperature distribution on the sample surfaces. Figure 15(b) shows the spectral radiation distribution curve corresponding to the position of the A-D coordinate points for the measured GH3030 alloy sample at a central heating temperature of 1173 K. The spectral intensity increased gradually as the measured point moved away from the center, indicating the surface temperature of the corresponding point gradually increased.

The spectral data cube of the measured GH3030 alloy sample was calculated using the narrow-band spectral window temperature inversion algorithm for multiple coordinate points along the X-axis (X=12.5, 25.0, 37.5, and 50.0 mm) and Y-axis (Y=10.0, 12.5, 15.0, and 17.5 mm). The obtained temperature distribution curves are shown in Figs. 16(a) and 16(b). The distribution of the measurements along the X- and Y-axes of the alloy sample shows that the

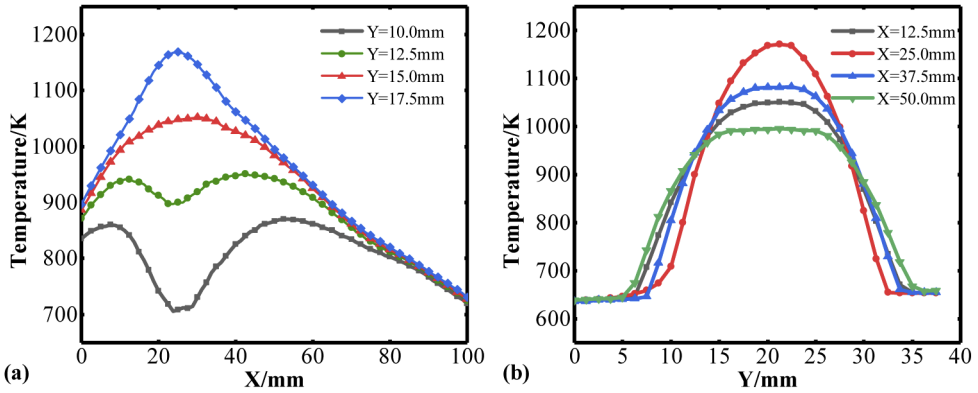

Fig. 16. The temperature distribution curve of the alloy sample under different (a) Y and (b) X coordinates at a core temperature of 1173 K.

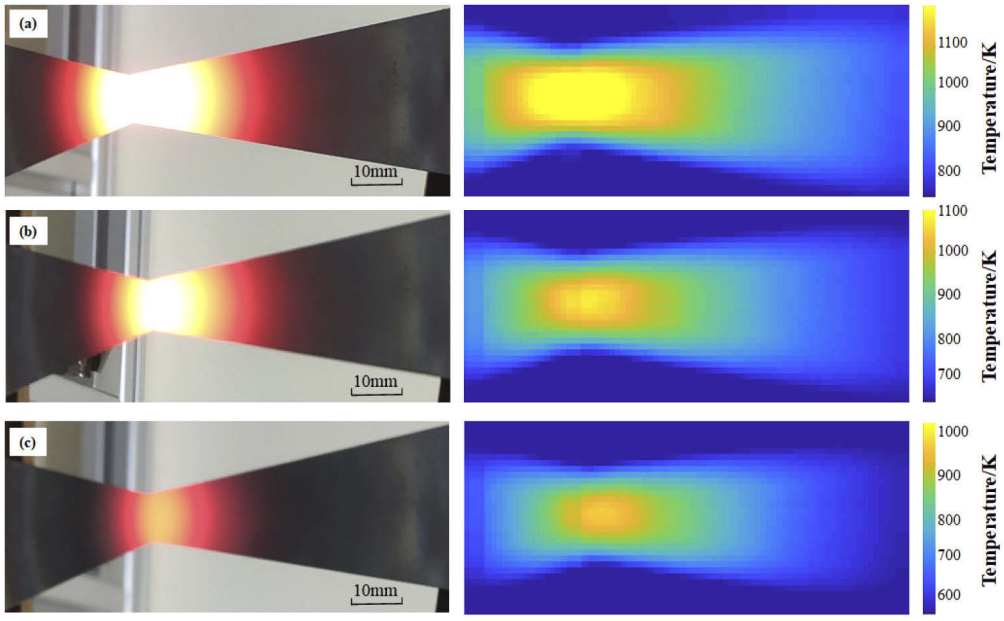

Fig. 17. (a) Original image and reconstructed temperature field distribution map of the alloy sample at a center temperature of (a) 1173 K, (b) 1073 K, and (c) 973 K.

Optics EXPRESS

closer the coordinates are to the center, the higher the temperature. Figures 17(a)–(c) show a physical map of the GH3030 alloy sample at temperatures of 973–1173 K and the reconstructed pseudo-color temperature field distribution after point-by-point scanning. The dovetail structure of the sample gives it a variable width along the longitudinal direction, where its narrowest part is in the middle and has the highest resistance. This changes the temperature field distribution on the surface due to different resistance distributions when heating. As the temperature near the center of the sample gradually increased, the brightness gradually increased and the reconstructed temperature field of the sample gradually decreased from the center to the sides.

5. Conclusion

A narrow-band spectral window moving temperature inversion algorithm that does not require an advanced setting of the emissivity model for the measured object is proposed using the principle of multispectral radiometric temperature measurements. Measuring the spectral radiation intensity of the object and fitting its profile using a narrow-band spectral window algorithm allows using the Mahalanobis distance coefficient to set the spectral inversion temperature at the closest distance to the narrow-band spectral window in the given temperature range. The simulation results show that the algorithm has a maximum relative error of 1.17% for temperature inversion at 20–30 dB of SNR. The surface temperatures for different types of nickel-based high-temperature alloy samples were experimentally measured with a maximum temperature measurement error of 1.33% compared with a reference thermocouple, which verifies the inversion accuracy of the algorithm. The spectral radiation intensity on the surface of the alloy sample was measured using the narrow-band spectral window algorithm to obtain the two-dimensional temperature field distribution for the GH3030 alloy sample. In summary, the narrow-band spectral window inversion algorithm ensures accurate temperature inversion without needing to preset the emissivity model. This provides new processing concepts for the practical application of turbine blade spectral temperature measurements, which can be applied not only in the field of turbine blades but also in other radiation temperature measurement fields, such as steelmaking.

Funding. National Natural Science Foundation of China (61727818, 61627819, 61805239); Jilin Scientific and Technological Development Program (20190303063SF; 20150520101JH, 20180201024GX,); Youth Innovation Promotion Association of the Chinese Academy of Sciences (2018254).

Disclosures. The authors declare no conflicts of interest.

References

1. I. Okada, T. Torigoe, K. Takahashi, and D. Izutsu, "Development of Ni base superalloy for industrial gas turbine," Super alloy **2004**, 707–712 (2004).
2. S. Garg, "Aircraft turbine engine control research at NASA Glenn Research Center," J. Aerosp. Eng. **26**(2), 422–438 (2013).
3. S. N. Zhao, X. F. Li, X. L. Huai, X. M. Zhou, and K. Y. Cheng, "The normal spectral emission characteristics of Ni-based alloys during oxidation at high temperatures," Int. J. Heat Mass Transfer **128**, 378–391 (2019).
4. T. Taniguchi, K. Sanbonsugl, Y. Ozaki, and A. Norimoto, "Temperature measurement of high speed rotating turbine blades using a pyrometer," in: *Proceedings of the ASME Turbo Expo 2006* 2, 521–529 (2006).
5. S. Kumari, D. V. V. Satyanarayana, and M. Srinivas, "Failure analysis of gas turbine rotor blades," Eng. Failure Anal. **45**, 234–244 (2014).
6. R. Dewangan, J. Patel, J. Dubey, P. K. Sen, and S. K. Bohidar, "Gas turbines blades critical review of failure on first and second stages," IJMERR **4**(1), 216–223 (2015).
7. Y. Lü, X. He, Z. H. Wei, Z. Y. Sun, and S. T. Chang, "Ambient temperature-independent dual-band mid-infrared radiation thermometry," Appl. Opt. **55**(9), 2169–2174 (2016).
8. H. Z. Zhu, Q. Li, C. Q. Zheng, Y. Hong, Z. Q. Xu, H. Wang, W. D. Shen, and M. Qiu, "High-temperature infrared camouflage with efficient thermal management," Light: Sci. Appl. **9**(1), 1–8 (2020).
9. Y. M. Ni, B. F. Zhang, H. T. Zheng, and L. X. Song, "Investigation on a laser-assisted radiation thermometry technique," Appl. Opt. **56**(16), 4654–4660 (2017).
10. S. Sade and A. Katzir, "Multiband fiber optic radiometry for measuring the temperature and emissivity of gray bodies of low or high emissivity," Appl. Opt. **43**(9), 1799–1810 (2004).
11. S. Gao, L. X. Wang, and C. Feng, "Multi-spectral pyrometer for gas turbine blade temperature measurement," Proc. SPIE **23**(1), 17–25 (2014).

Optics EXPRESS

12. A. L. Sahlberg, D. Hot, R. Lyngbye. Pedersen, J. Zhou, M. Aldén, and Z. Li, "Mid-infrared polarization spectroscopy measurements of species concentrations and temperature in a low-pressure flame," Appl. Spectrosc. **73**(6), 653–664 (2019).
13. J. Liang, L. Dai, S. Chen, W. Gu, B. Peng, N. Jiang, W. Song, and J. Xing, "Generalized inverse matrix-exterior penalty function (GIM-EPF) algorithm for data processing of multi-wavelength pyrometer(MWP)," Opt. Express **26**(20), 25706–25720 (2018).
14. J. Xing, B. Peng, Z. Ma, X. Guo, L. Dai, W. Gu, and W. Song, "Directly data processing algorithm for multi-wavelength pyrometer (MWP)," Opt. Express **25**(24), 30560–30574 (2017).
15. T. R. Fu, P. Tan, C. H. Pang, H. Zhao, and Y. Shen, "Fast fiber-optic multi-wavelength pyrometer," Rev. Sci. Instrum. **82**(6), 064902 (2011).
16. J. Estevadeordal, G. H. Wang, N. Nirmalan, A. Q. Wang, and T. D. Rigney, "Multicolor techniques for identification and filtering of burst signals in jet engine pyrometers," J. Turbomachinery **136**(3), 031004 (2014).
17. H. W. Liu, S. Zheng, and T. Y. Wang, "Experimental study of radiation characteristics and temperature distributions of gasoline and biomass flame," IET Renewable Power Generation **13**(11), 1833–1839 (2019).
18. D. Ketui, F. Chi, and G. Shan, "Single wavelength and ratio pyrometry reflection errors in temperature measurement of gas turbine blade," Measurement **86**, 133–140 (2016).
19. B. Bouvry, G. Cheymol, L. Ramiandrisoa, B. Javaudin, C. Gallou, H. Maskrot, N. Horny, T. Duvaut, C. Destouches, L. Ferry, and C. Gonnier, "Multispectral pyrometry for surface temperature measurement of oxidized Zircaloy claddings," Infrared Phys. Technol. **83**, 78–87 (2017).
20. J. Manara, M. Zipf, T. Stark, M. Arduini, H. P. Ebert, A. Tutschke, A. Hallam, J. Hanspal, M. Langley, D. Hodge, and J. Hartmann, "Long wavelength infrared radiation thermometry for non-contact temperature measurements in gas turbines," Infrared Phys. Technol. **80**, 120–130 (2017).
21. P. Wang, Z. W. Hu, Z. Xie, and M. Yan, "A new experimental apparatus for emissivity measurements of steel and the application of multi-wavelength thermometry to continuous casting billets," Rev. Sci. Instrum. **89**(5), 054903 (2018).
22. J. Y. Lin, X. Y. Zhang, K. Y. Liu, and W. J. Zhang, "Emissivity Characteristics of Hydrocarbon Flame and Temperature Measurement by Color Image Processing," Energies **12**(11), 2185 (2019).
23. Y. Z. Zhang, W. Q. Zhang, Z. Dong, S. B. Shu, X. L. Lang, and L. Yang, "Measurement performance analysis for a charge-coupled-device-based near-infrared multi-spectral pyrometer," Infrared Phys. Technol. **106**, 103273 (2020).
24. W. J. Yan, A. Panahi, and Y. A. Levendis, "Spectral emissivity and temperature of heated surfaces based on spectrometry and digital thermal imaging–Validation with thermocouple temperature measurements," Exp. Therm. Fluid Sci. **112**, 110017 (2020).
25. Y. P. Sun, C. Lou, and H. C. Zhou, "A simple judgment method of gray property of flames based on spectral analysis and the two-color method for measurements of temperatures and emissivity," Proc. Combust. Inst. **33**(1), 735–741 (2011).
26. W. J. Yan, H. C. Zhou, Z. W. Jiang, C. Lou, X. K. Zhang, and D. L. Chen, "Experiments on measurement of temperature and emissivity of municipal solid waste (MSW) combustion by spectral analysis and image processing in visible spectrum," Energ," Fuel **27**(11), 6754–6762 (2013).
27. S. Gao, L. X. Wang, C. Feng, and K. Daniel, "Analysis and improvement of gas turbine blade temperature measurement error," Meas. Sci. Technol. **26**(10), 105203 (2015).
28. S. Deep, Y. Krishna, and G. Jagadeesh, "Temperature characterization of a radiating gas layer using digital-single-lens-reflex-camera-based two-color ratio pyrometry," Appl. Opt. **56**(30), 8492–8500 (2017).
29. J. J. Talghader, A. S. Gawarikar, and R. P. Shea, "Spectral selectivity in infrared thermal detection," Light: Sci. Appl. **1**(8), e24 (2012).
30. C. D. Wen, "Investigation of steel emissivity behaviors: Examination of Multispectral Radiation Thermometry (MRT) emissivity models," Int. J. Heat Mass Transfer **53**(9-10), 2035–2043 (2010).
31. Z. Yuan, J. Zhang, J. Zhao, Y. Liang, and Y. Duan, "Linearity study of a spectral emissivity measurement facility," Int. J. Thermophys. **30**(1), 227–235 (2009).
32. K. H. Zhang, K. Yu, Y. F. Liu, and Y. J. Zhao, "An improved algorithm for spectral emissivity measurements at low temperatures based on the multi-temperature calibration method," Int. J. Heat Mass Transfer **114**, 1037–1044 (2017).
33. B. Kong, T. Li, and Q. Eri, "Normal spectral emissivity measurement on five aeronautical alloys," J. Alloys Compd. **703**, 125–138 (2017).
34. F. Zhang, K. Yu, K. H. Zhang, Y. L. Liu, Y. J. Zhao, and Y. F. Liu, "Infrared spectral emissivity property of pure titanium in the 473–1035 K temperature range," Appl. Spectrosc. **70**(10), 1717–1725 (2016).